Master STEP

GÉOPHYSIQUE

Broadband interferometry imaging of the rupture complexity of the Mw 8.8 2010, Maule and of the Mw 8.6 2012, Sumatra earthquakes

Eszter KIRÁLY

Résumé

Broadband analysis of large earthquakes can reveal new elements about complex source properties and post-seismic activity. Combined investigation of high- and low-frequency energy radiations can improve our understanding on rupture mechanism, propagation, seismic nucleation properties and give new information to estimate seismic potential of different regions.

In this study two large earthquake were analysed: the 27 February 2010 Maule earthquake (Mw 8.8) and the 11 April 2012 Sumatra earthquake (Mw 8.6). For the Maule earthquake, a back projection analysis the frequency range of 0.1-3Hz together cGPS data at the northern end of the rupture shows particular pattern: low- and high-frequency co- and post-seismic radiation encircles a strongly coupled area, where two years later the 25 March 2012 aftershock (Mw 7.1) broke and released at least a part of the accumulated stress. The 2012 Sumatra earthquake was the biggest ever recorded intra-plate strike-slip earthquake occurred this April offshore from Sumatra. Back projection and surface wave analysis showed that complex west-ward propagating sequence dynamically triggered inherited NNE-SSW left-lateral strike-slip oceanic fabrics.

Mots clés : broadband, rupture complexity, Maule, Sumatra

Contents

1   Introduction

Earthquakes occur all over the world with different focal mechanisms, magnitudes and at various geodynamical situations. Large earthquakes are quite common around tectonic plate boundaries, especially in subduction zones, however intraplate deformation also could produce high magnitude events (e.g. 2012 Sumatra). The 2011 Tohoku earthquake [Satriano et al., 2011] demonstrated that in the case of extended ruptures observed high-frequency radiation is not necessary co-located with large coseismic slip asperities reflecting complexities of rupture process, heterogeneities of mechanical and geometrical parameters of the source.

At the first decades of instrumental seismology, only location and magnitude of large events could be identified apart from field observations of shaking and tsunami destructions. Developments of slip inversion techniques significantly promoted seismic investigations since they give information about among others fault geometry, slip distribution in the plane. Nevertheless, it has to be noted that results highly depend on a priori information, e.g. orientation of the fault, and they give insight only into a small portion of the rupture process. During the last decade, back projection methods were developed in order to image the coherent energy radiated by the rupture. Back projection gives independent point of view – with minimal bias – about large earthquake rupture properties. Combination of long-period GPS measurements and surface wave analysis with back projection at higher frequency bands can provide new insights into rupture dynamics.

This study focuses on two great earthquakes from different regions. First area is the Chilean subduction zone where several large, mainly thrust earthquakes occur regularly such as the 27 February 2012 Maule event. Since this event occurred two years ago, several studies were published using different methods such as GPS, InSAR, teleseismic, back projection. However, there are still open questions about the rupture propagation and ending to the north as well as to the south.

The second region is located in the diffuse inner-plate boundary between the Indian and Australian parts of the Indo-Australian plate. The majority of earthquakes are strike-slip events as the Mw 8.6 earthquake, occurred close to the coast of Sumatra in April 2012, and followed by a Mw 8.2 aftershock in 2 hours. Since this event is very recent and the seismotectonics of area is still not well-understood, the aim of this study was to describe the kinematics of the rupture propagation and find explanation what kind of structure broke during the earthquake.

The following is structured into two main chapters. Chapter 2 deals with the Maule earthquake, which is presented in light of the geodynamic context of Chilean subduction and studied through combined back projection and cGPS analysis. Chapter 3 presents the results of combined back projection and surface wave analysis on the 2012 Sumatra earthquake. The chapter is structured after a paper [Satriano et al., 2012] which is currently in press at Geophysical Research Letters.

2   Broadband study of the northern termination of the 27 February 2010 Maule earthquake (Mw 8.8) rupture

2.1   Geodynamic setting

Chile is one of the most active seismic areas in the world. The Nazca plate started to subduct under the South American plate 3Ma ago creating mountain ridges of the Andes. The plates converge about 70mm/yr in the direction of N78^o [Vigny et al., 2009]. Due to the relatively fast convergence large amount of earthquakes occurs yearly, and events with about Mw

8 happen every 10 years [Madariaga et al., 2010]. Thanks to historians and seismologists, the seismicity of Chile is relatively well-known [Beck et al., 1998], [Lomnitz, 2004]. According to these works, this subduction zone appears fragmented in several 100-200km long and 50-100km wide segments which may be at different stage of the seismic cycle. Lifetime of the segments is not clear, whether they are permanent features or only transient. The Maule segment (35ºS-37ºS) is situated in Central Chile where the last earthquake occurred in 1835 as reported by Darwin. Seismicity of this region was unusually low since at least 1976 [Campos J.and Hatzfeld et al., 2002], thus detailed seismic studies were not possible [Madariaga et al., 2010]. On the other hand, based on analysis of interseismic survey GPS measurements, Ruegg et al. [2009] pointed out that the segment is strongly coupled and there is a high probability of a large earthquake in the area. They report velocities in convergence direction of Nazca plate with respect to the stable South American plate. Magnitude of velocities decrease rapidly towards the east suggesting elastic deformation locked till the depth of about 60km. As a consequence, they warn that this strain accumulation over a mature seismic gap could create large (Mw 8) earthquake in the near future.

During the 20th century two big earthquakes occurred in the segment: the 1928 Talca was a shallow underthrusting event, ruptured less than 150km of the interface and did not release significant energy. The other earthquake occurred in the subducting slab (Chillian 1939) which did not released the accumulated stress either [Beck et al., 1998]. The most powerful event ever recorded in the world occurred near Valdivia in 1960 (Mw 9.5) at the south end of the Maule segment causing great tsunami, landslides and flood damage [Lomnitz, 2004]. On the northern edge of the segment, the Valparaíso event (Mw 8.0) occurred in 1985 [Comte et al., 1986]. However, a large area between these latter events remained unbroken since 1835.
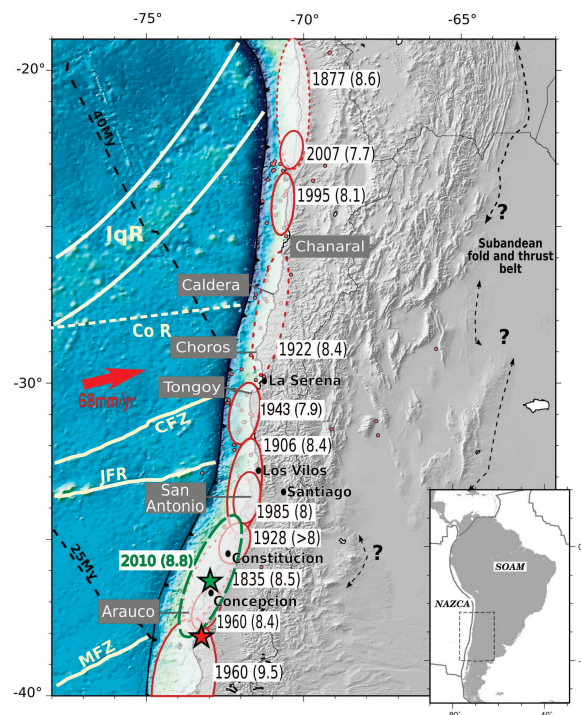

Figure 1 – Historical earthquakes of the Maule segment during the last two centuries [Métois et al., 2012]

An important feature of the Chilean subduction zone is, that the trench is close to the coast (100-150km). As a consequence, GPS measurements can detect not only horizontal but

vertical displacements as well since hinge line is onland [Métois et al., 2012]. Moreover, GPS network has a good resolution on slip which may occur not far from the trench.

Ruegg et al's forecast came true with the Maule earthquake on 27 February 2010 at 06:34:14 UTC. The hypocenter is located at 35.909^o, 72.733^oW, at 35km depth. Focal mechanism (strike=19°, dip=18°, slip=116° from Harvard CMT catalog) shows a thrust event corresponding to the frictional motion of the overriding plate over the subducting one. Thanks to modern earthquake-resistant buildings, rapid reaction of the population in contempt of the lack of earthquake-proof communication the official toll of victims is about 500, which is a small number compare to other events [Madariaga et al., 2010].

Researchers agree that this event ruptured bilaterally and large slip took place in the north (34°-35°) reaching the max value of 20m. However, there are debates about the nature of the southern patch, localized [Delouis et al., 2010] or uniformly distributed [Tong et al., 2010]; and about location of significant slip along dip: some authors place significant slip close (0-50km) to the trench [Vigny et al., 2011], [Lay et al., 2010] while others localize it farther (50-150km) from the trench [Lorito et al., 2011], [Delouis et al., 2010]. Several geodetic investigation agree that coseismic slip occurred during the Maule earthquake filled the Conceptión-Constitutión seismic gap [Moreno et al., 2012], [Vigny et al., 2011]. Lorito et al. [2011] based on slip distribution model from joint inversion of tsunami and geodetic datasets agree that the most of the high-slip region corresponds to relatively high coupling zones. However, they show that the high pre-seismic locking zone around 38.5^o-36^oS remained unbroken, and not only did not rupture completely the gap but this event produced a strong increase in stress in highly locked zones, increasing the possibly of significant earthquakes in the Darwin-gap. They warn that high interseismic coupling is necessary but not sufficient condition for high slip in a single event, one has to take into account additional effects of fault rheology, structural heterogeneities and slip history on the fault. On the other hand, Moreno et al. [2012] inferred that studies with a denser set of near field GPS measurements find opposite conclusion, that is, the Darwin-gap is filled by the Maule event.

Dense near-field GPS observations [Vigny et al., 2011] of the subsequent 12 days show less afterslip near Constitution where coseismic slip was larger, however they obtained significant afterslip to the north where coseismic slip was small. Directions of afterslip and coseismic movements are not parallel, which might indicate that postseismic activity on different patches. Observation of large inland post-seismic deformation may indicate that post-seismic activity took place under the seismogenic zone.

According to Rietbrock et al. [2012] aftershocks are located about 50-140km from the trench, at about 10-35km depth. Location of aftershocks is governed by rupture process of the main shock and static stress change. If main shock releases a large fraction of interseismic strain [Rietbrock et al., 2012], aftershocks seem to occur in areas of rapid transition between high and low slip [Das and Henry, 2003]. Vigny et al. [2011] propose that coseismic slip was release close to the trench, which has a good correlation with the location of aftershock activity. However, relation of coseismic slip and aftershocks is not fully understood since it depends significantly on the slip model.

Increased activity was reported at several clusters (Figure 2). 40-45km depth: events might be driven be afterslip since high post-seismic activity and a downdip of the coseismic rupture are observed [Lange et al., 2012], beneath active volcanic front, on the outer rise of Nazca plate to the North. One of the biggest aftershocks corresponds to crustal normal faulting in the overriding plate. Two big events occurred at Pichilemu [Ryder et al., 2012] on a $N145^o$ striking SW dipping fault. They caused significant seismic hazard since these event are situated close to inhabited areas and they performed relatively strong ground motion. Ryder et al. [2012] found that these earthquakes have been triggered by static stress changes from the
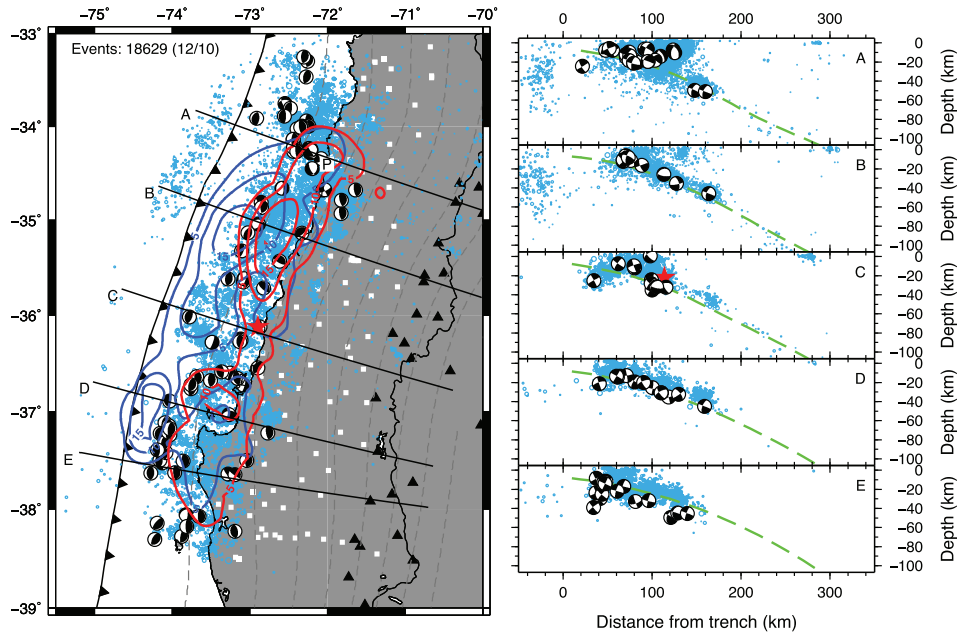
Figure 2 – Aftershock distribution (blue dots) after the main event [Rietbrock et al., 2012] . 5m slip contours based on the slip model of Vigny et al. [2011] and Lorito et al. [2011] are shown in blue and in red, respectively. Trench perpendicular lines define the location of cross sections (right panels)

main shock. Several studies pointed out that this event not only filled a large seismic gap, but rupture endings overlap with previous earthquake areas (e.g. [Métois et al., 2012]. However, terminations of the rupture both in the south and in the north are not well-understood. The main question is where the rupture has stopped. Investigation on the southern part was not possible because of lack of resolution. However, back projection analysis (as will be presented below) combined with cGPS observations allow to better understand the rupture termination on the northern part. This is crucial to evaluate actual seismic risk in Central Chile.

2.2 Back projection method

Back projection is a new technique which enables to image complex earthquake sources. The goal of back projection is to search for coherent radiation sources in space and in time in a grid fixed around the hypocenter in order to provide information about spatio-temporal evolution ofthe earthquake rupture. The greatest advantage of this signal processing method is that it requires only hypocenter parameters as a-priori knowledge, hence it can be applied almost real time [Ishii et al., 2005a]. Another significant advantage is the fact that back projection is a completely independent approach compared to inversion techniques, not depending on a priori parameters, e.g. rupture velocity. This method is able to give new insights to source investigation with minimal bias.

Back projection resolution depends on array geometry and orientation. To be able to focus on higher frequencies, dense array configuration is needed. However narrow aperture of the array decreases resolution for lower frequencies. Moreover, the physical interpretation of seismic energy back projection is not clear. The method allows to track only coherent radiation of the total energy field. This means that radiation is possible, although at a reduced level, even in areas where back projection does not indicate energy.

In the process, the first step is beam forming. A two-dimension grid is considered with

regularly spaced points in latitude and longitude around the hypocenter. At each grid point theoretical arrival times are calculated to each seismometer in the array using the AK135 radial Earth model [Kennett et al., 1995], a time window of the normalized data is extracted around a certain arrival and data segments are stacked in to a beam. In this study we used P-waves since they are easy to detect and they are not contaminated with other phases. Then beam power is calculated at each grid point with both N1 root stacking and N4 root stacking. (Equations are reported in the Appendix.) At each grid point, beam power is measured and mapped back to the grid point. This process is repeated for each time step. As a result, regions of high beam power are mapped in time and space. These regions are indicative of constructive radiation [Ishii et al., 2005b].

Nth root stacking is applied to suppress spikes, glitches, noise and enhance seismic signal on the traces. N1 stacking gives the truest amplitudes but resolution is poorer [Xu et al., 2009]. N4 stacking – sensible for phase information – suppresses noise efficiently, resolution is better but amplitude distortions are involved. In order to account for unmodeled lateral velocity heterogeneities, station corrections are calculated by multi-channel cross-correlation alignment [Vandecar and Crosson, 1990a].

Back projection resolution depends on the array geometry, and can be quantified for each frequency by the array response function (ARF) [Rost and Thomas, 2002].

Calibration of back projection image is verified with aftershocks. The objective is to check whether aftershocks are correctly back projected at their hypocenter using the station correction calculated for the main shock. If that is not the case, further corrections should be applied across the grid. Spatially well-distributed aftershocks with 5.0<Mw<6.5 are good candidates for calibration. They need to be quite energetic to be able to back project their radiation; on the other hand, they should not be larger than Mw 6.5 meaning that they could be considered as point sources at teleseismic distances, thus rupture propagations are negligible.

Array geometry can introduce distortions in the back projection image. Weighting according to spatial distribution of the stations is able to correct these artifacts. It is defined by the area of voronoi cells around each station. Voronoi cells of densely located stations are suppressed whereas sparse location get higher weight clearly developing back projection image (Figure 4).

Destructive interference sweeping through the back projection image (in optic Moiré-effect, here it is called "swimming effect") is an artifact of antenna methods. This effect can be mitigated by smoothing. A space-time smoothing operator published by Walker and Shearer [2009a] is used to post-process back projection image keeping the energy at slow speeds and attenuating artifacts (Figure 4). A local maximum filter is used to detect peaks of radiation energy at each time step.

Results of back projection can be presented with time integrated images. These figures are calculated by the integral of beam power over a certain time (INT) or maximal values of the beam power are associated to the grid points (MAX). (Equations are reported in the Appendix.) Propagation of radiation is imaged by the space-time evolution of maximum peak values.

2.3 Data and results

For this study, data were provided by the transportable array of the USA (USArray) 280 vertical velocity traces of the 2010 geometry were used for this back projection analysis. USArray is situated at the epicentral distance of 60°- 90° north from the Maule hypocenter.

Spectrum analysis of the whole dataset reveals the value of corner frequency (about 0.07Hz) and the strongly attenuated high frequency content from 3Hz. Spectrum between these
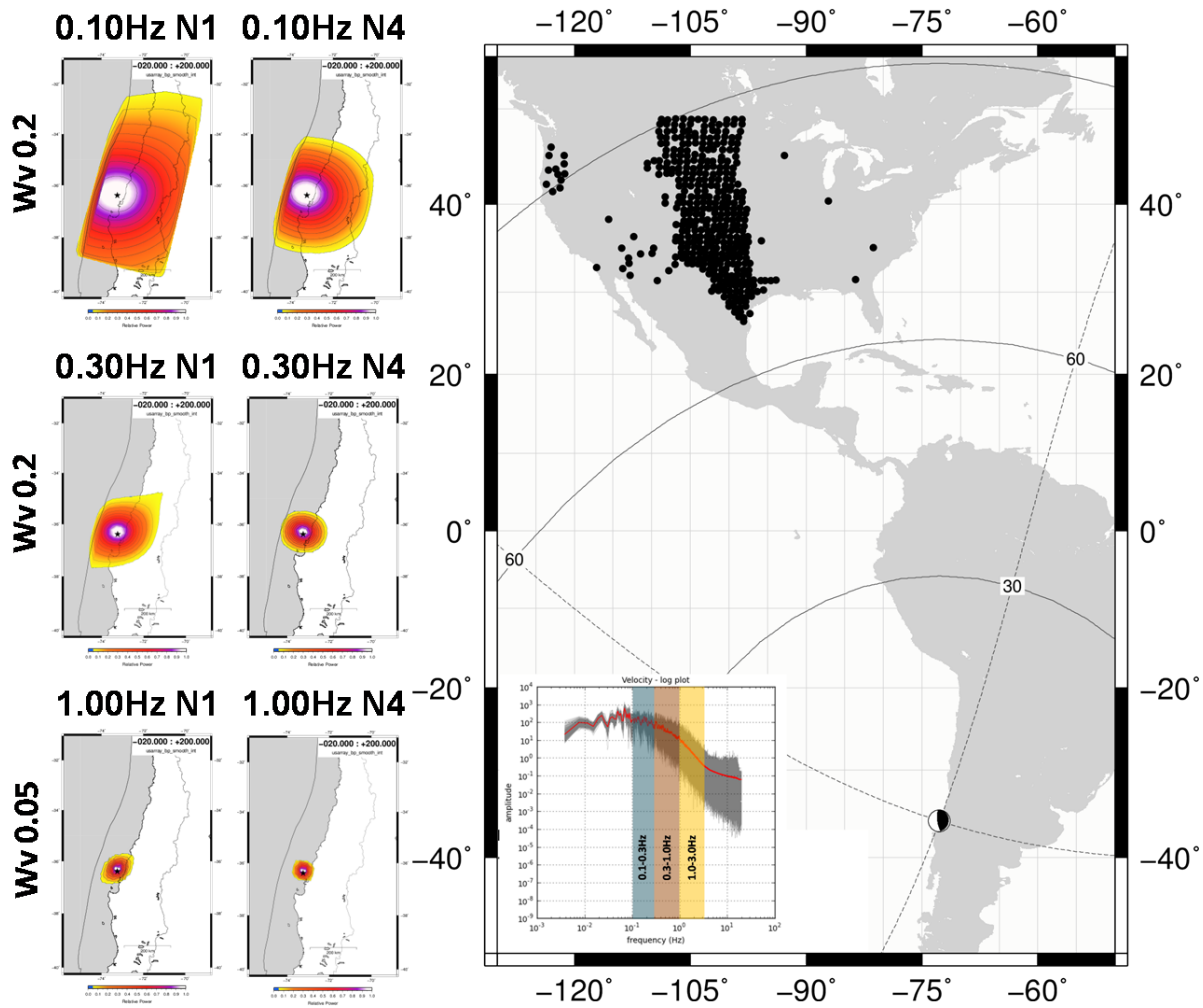
Figure 3 – Resolution tests of the USArray (ARF) at all frequency bands (left panels), geometry and location of the USArray with respect to the Maule hypocenter (right panel). Inset shows the frequency content of the main shock

values is divided into three bands: 0.1-0.3Hz (low frequency band), 0.3-1.0Hz (intermediate frequency band), 1.0-3.0Hz (high frequency band) (Figure 3 bottom right). Filtering was carried out with four-pole noncausal Butterworth filter.

   ARFs are calculated for N1 and N4 stacking separately at each frequency band (Figure 3). ARFs are constructed with back projection of monochromatic signals with the dominant frequencies for each frequency band which are always the lowest frequencies (0.1Hz, 0.3Hz, 1.0Hz for 0.1-0.3Hz, 0.3-1.0Hz and 1.0-3.0Hz frequency bands, respectively). This analysis allows to estimate the lowest resolution limit. Resolution tests show that the higher the frequency, the higher the precision. Resolution of N4 stacking is generally better than that of N1 stacking: the spots are more constrained and do not display distortions in the direction of the USArray (Figure 3). This is because N4 stacking enhances phase coherency over amplitude coherency.

   Back projection is performed over a grid laid around the epicenter on the interface between the overriding and subducting plates. The grid is 400km wide and 800km length plunging towards east with 18°, rotated with 15° to the east. Main shock coordinates are provided by SSN (Servicio Sismológico Nacional, Chile): 36.290ºS, 73.239ºW, 30.1km depth 06:34:08 UTC. Seismogram traces are stacked over 220s, starting from 20s before the first arrival.
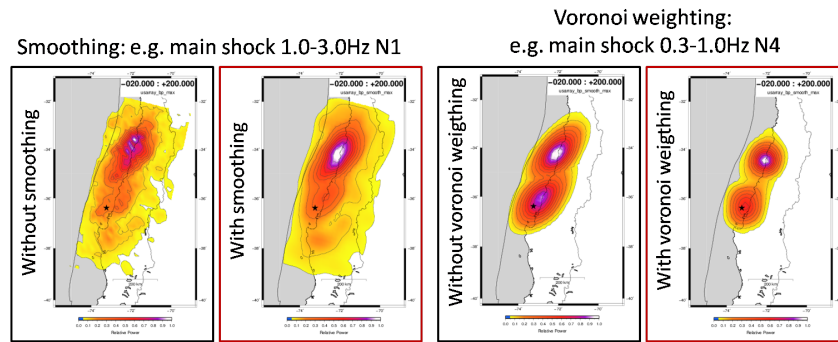
Figure 4 – Effects of smoothing (left panels) and voronoi weighting (right panels)
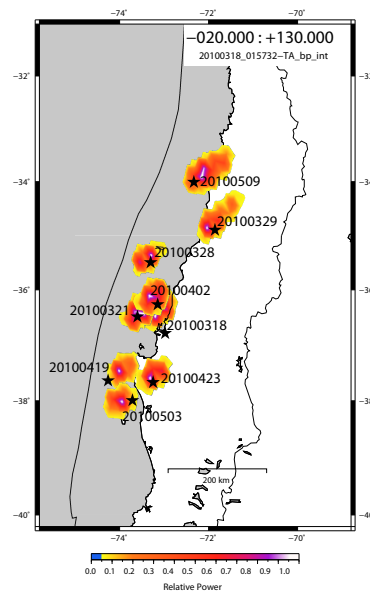

Figure 5 – Results of calibration. Black stars indicate the aftershock hypocenters, redish-yellowish spots show the back projections using the station corrections of the main shock

Calibration of the main shock is carried out with 9 aftershocks which are spatially well-distributed. Results of calibration (Figure 5) applying N4 stacking show back projection spots close to the epicenters (provided by Rietbrock et al. [2012]), within a few tens of km. Higher deviations are indicated in the case of less energetic (Mw 5.2) sources. The most pronounced errors, which are the case of the 18 March 2010 and the 19 April 2010 aftershocks, remain still quite small and back projection of aftershocks are satisfying. Thus, back projection of the main shock is reliable all over the grid.

As many previous studies, results show bilateral energy propagation with a stronger north component (Figure 6). Coherent energy propagates essentially along strike, only slight variations are observed along dip. Northern part of the propagation is evident in each frequency band both with N1 and with N4 stacking. On the other hand, southward propagation can be seen only in the intermediate and high frequency band. Even if N1 stacking images are generally noisier, southward propagation is more visible. In the same time, N4 stacking figures present two high radiation spots: one around the epicenter and one about 300km northern along the coast, but no clear evidences to southward motion are shown.

Low frequency band (Figure 6 top) presents one energy spot towards the north both
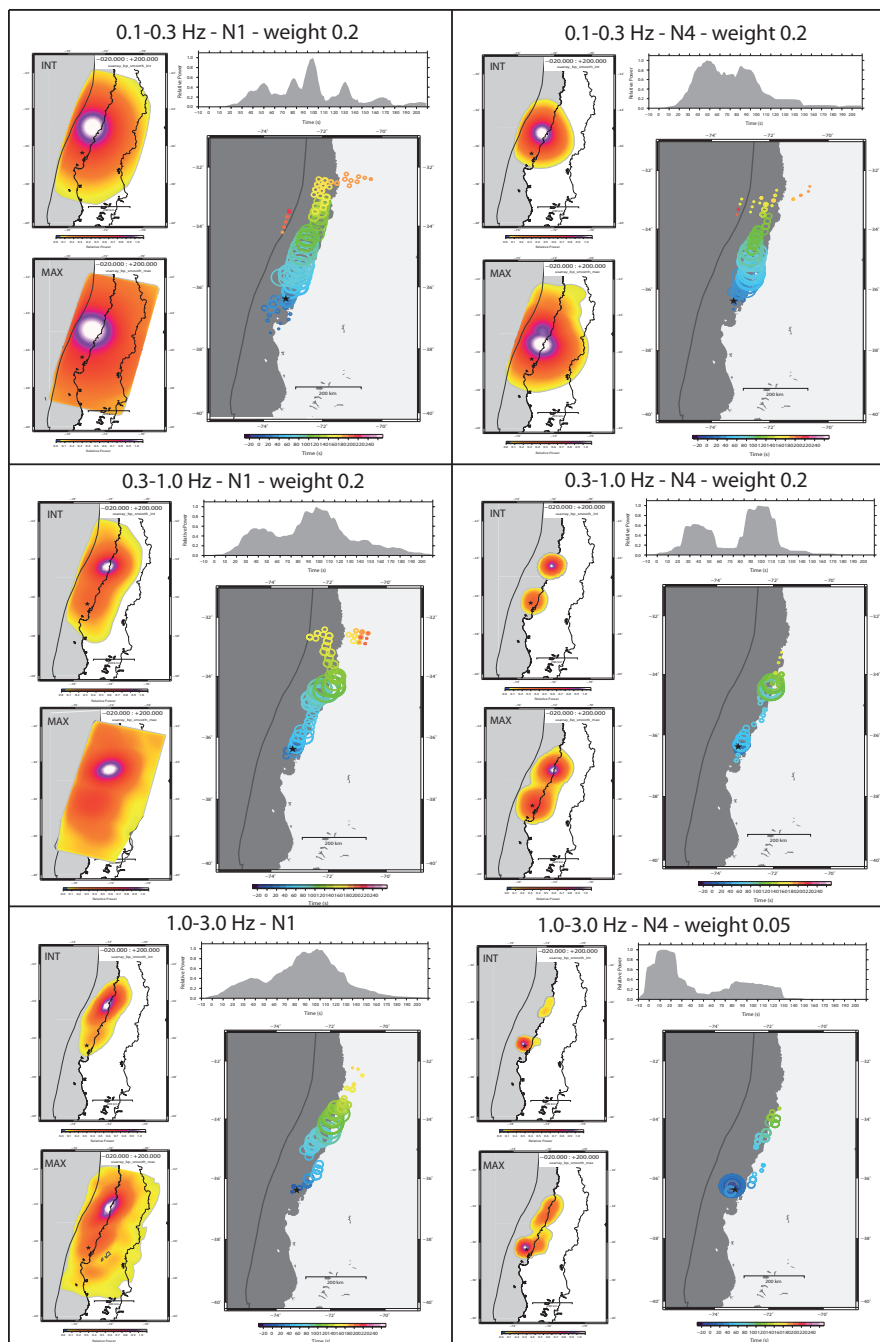
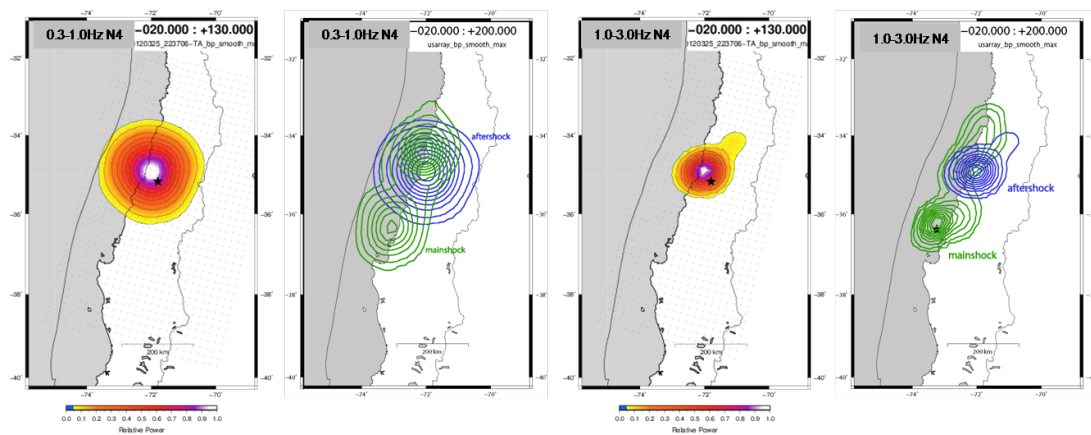Figure 6 – Results of back projection at all frequency bands using N1 ans N4 stacking

Figure 7 – Back projection of the 25 March 2012 aftershock in the frquency ranges of 0.3-1.0Hz and 1.0-3.0Hz. Superposition of main shock (green contours) and aftershock (blue contours) show their relative position

in N1 and N4 stacking, since array has low resolution at that frequency band. In order to improve this resolution, array aperture should be widened. Resolution of intermediate and high frequency band (Figure 6 middle, bottom) is high enough to localize 2 separated coherent energy spots: one around the hypocenter, the other about 250km north from the epicenter. In these frequency bands, highest relative coherent energy burst is located at the northern patch generally, however N4 stacking of high frequency band locate it around the hypocenter.

The preferred solution, discussed in the next section is the intermediate frequency band with N1 stacking, since the image is consistent N4, with good resolution, and amplitudes are not distorted.

An important aftershock occurred on 25 March 2012 (Mw 7.1) 200km NNE from the main shock epicenter (35.183^oS, 71.792^oW, 34.8 km depth). This was the strongest event since February 2010. Analysis of this aftershock can give some new elements to understand broadband properties of the seismic activity of the region. Back projection of this event was carried out in the same frequency bands as the main shock (0.3-1.0Hz and 1.0-3.0Hz) in order to be able to compare the results. Since this earthquake occurred 2 years later, when USArray was already displaced, this aftershock is back projected with the 2012 configuration of the transported array. Figure 7 show that this earthquake broke between the two high radiation patches of the main shock, closer to the northern one. These results are also incorporated in the broadband comparison below and will improve the understanding on the seismic activity of the Maule segment.

2.4   Discussion

2.4.1   Comparison with previous back projection studies

Back projection results of Kiser and Ishii [2011] show southward propagation at the beginning on the southern segment and on a third segment located around 37.5^oS at the end of the coseismic slip while our results do not indicate high radiating spot at the south. Moreover, their evolution of high radiating peaks indicates downdip propagations of both segments which could be due to the lack of calibration and appropriate spatial weighting of stations. Tests of voronoi weighting explain that it significantly improves the back projection image at almost every frequency band: radiation peaks are more constrained, their elongated shape
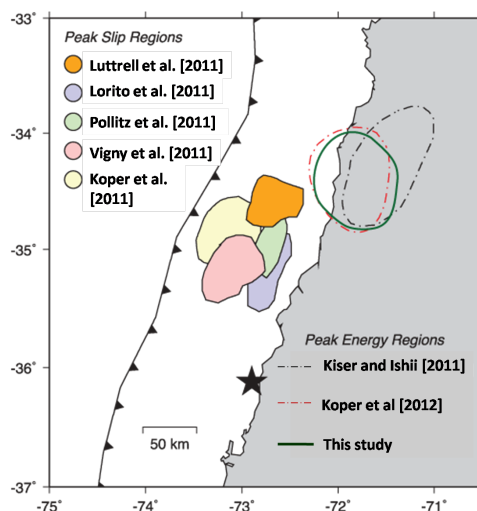
Figure 8 – Comparison of previous geodetical and back projection results, after Koper et al. [2012]

become circular and radiation propagates principally along strike with a very small dipward component. However, one has to be careful with the voronoi weighting at high frequencies (1.0-3.0Hz) using N1 stacking. Since amplitudes at high frequencies are sensitive to local heterogeneities and variations of the structure of the Earth, these amplitudes can be coherent at densely spaced stations. Thus, giving too significant weight to dispersed and separated stations introduces secondary maxima artifacts.

Kiser and Ishii [2011] proposed rupture jump between the southern and northern segments, however our results cannot confirm it. One can observe two main patches but energy moves with continuity from the south to the north, without significant jump.

Koper et al. [2012] compared back projection results to finite fault slip models (Figure 8). They calculated high energy radiation areas from North American, Japan, European arrays as well as global network. They found that short period radiation is located between 34°- 35^oS and 72.5^o- 71.5^oW. This location overlaps with the high frequency radiation spot obtained by Kiser and Ishii [2011], but not entirely because of the before mentioned lack of spatial weighting in the study of Kiser and Ishii [2011]. On the other hand, short-period radiation location of this study corresponds exactly to that of Koper et al. Their slip distribution corresponds well to other previous studies revealing frequency dependence along dip: in general large coherent slip is in the updip region closer to the trench, while short-period waves are radiated dowdip.

Dionicio et al. [2012] calculated slip distribution with kinematic inversion of teleseismic waves in 0.03-1.0Hz. They modeled rupture propagation as a circle concentrically growing from the epicenter on the fault plane. According to their model, slip starts around the hypocenter, continues bilaterally with a major northern and minor southern component till 80s. Then slip propagates exclusively northward then disappears around 120s. Finally, a small secondary patch appears between 150s and 190s around 35^oS. Strong slip located always closer to the trench. Comparing to back projection results (0.3-1.0Hz) one can observe again the spatial separation of different frequency radiations: large slip is located trench-ward with respect to coherent high-frequency energy radiation.

According to Lay et al. [2012a], depth-dependence of rupture properties, especially frequency-dependence of seismic energy radiation is not unique for Chile, it rather seems to be systematic in several subduction zones. Coherent teleseismic high-frequency energy radiates from the deeper part while large slip occurs at the shallower portion of the megathrust. They

separated four regions on the subduction interface in function of dip. The shallowest 15km is the region of tsunami earthquakes (domain A), 15-35km deep large coseismic slip occurs radiating small amount of coherent high-frequencies (domain B). Smaller isolated megathrust patches rupture between 35km and 55km depth (domain C). Breaking of these isolated patches produce coherent short-period energy release in great ruptures as well as in moderate size events. Going deeper, at depth of 30-45km (domain D) low-frequency earthquakes, seismic tremors and slow slip events present the transition zone between the seismogenic zone and the stable sliding or ductile flow.

2.4.2 Comparison of energy radiation and geodetic displacement

On the Figure 9 A GPS motogram vertical traces are plotted in function of distance from the hypocenter. Data were used only from GPS stations which are close to the coast. First arrivals indicate a velocity of about 3.7km/s, corresponding to Rayleigh wave. At close stations (closer than 350km): GPS data shows that 15s after the first arrival an abrupt signal level change which means that static field is installed. Farther stations (more than 400km away from the hypocenter) do not indicate static field installation. This suggests that rupture front arrives almost immediately after the first Rayleigh wave propagating till 350km far from the hypocenter, then Rayleigh wave propagates further to the north but rupture stopped.

Figure 9 C integrates the two observables: low-frequency first arrivals at GPS stations (blue squares) and high-frequency (0.3-1.0Hz) radiation maxima (red dots). Horizontal axis indicates the elapsed time with respect to the hypocenter time of the main shock, vertical axis shows along-strike distances of either GPS stations or radiation peaks to the main shock epicenter. Note that distances are calculated with respect to SSN hypocenter and distances to stations located southern from the main shock are given by negative values.

Rupture front and high-frequency radiation are together till 70s, however, at that moment, radiation of high frequencies uncoupled from the rupture front and stucks at the area while slip runs rapidly toward the north. This does not necessarily imply that rupture front is not emitting high-frequency radiation, but rather that this is not the dominant high frequency imaged by back projection. The source of this high level coherent short-period radiation could be breaking of small asperities around a strongly coupled patch which is not able to break. After about 30s, high-frequency starts to move further to the north along the strike with the same velocity as before. It stops again around 350km where at first high relative energy amount is released than radiation diminishes and dies away. This area corresponds well to the end of the rupture.

Coseismic slip close to the trench, short-period radiation of the main shock and post-seismic slip of the subsequent 12 days (located down-dip) encircle an area which seems to be stable (Figure 9 B), and which has been possibly charged during the coseismic period. The strongest aftershock of the Maule earthquake broke this area on 25 March 2012. It propagated northward and downdip where no significant co- or post-seismic slip occurred before. Thus, since coseismic charging of the asperity was not released during the afterslip, moreover, post-seismic activity also recharged the area, breaking up of the coupled patch created a strong Mw 7.1 earthquake (Figure9 B).

In future works, in order to better understand the northward ending of the rupture, a better resolution of static deformation should be evaluated. It would be necessary to analyze cGPS data filtered at higher frequencies (around 5-10s periods) and compare it to results of other frequency bands. Since back projection of coherent high frequency energy can vary depending on the array position with respect to the source and the array geometry, analysis of the coseismic teleseimic traces of other arrays (e.g. European array) would improve the back pro-
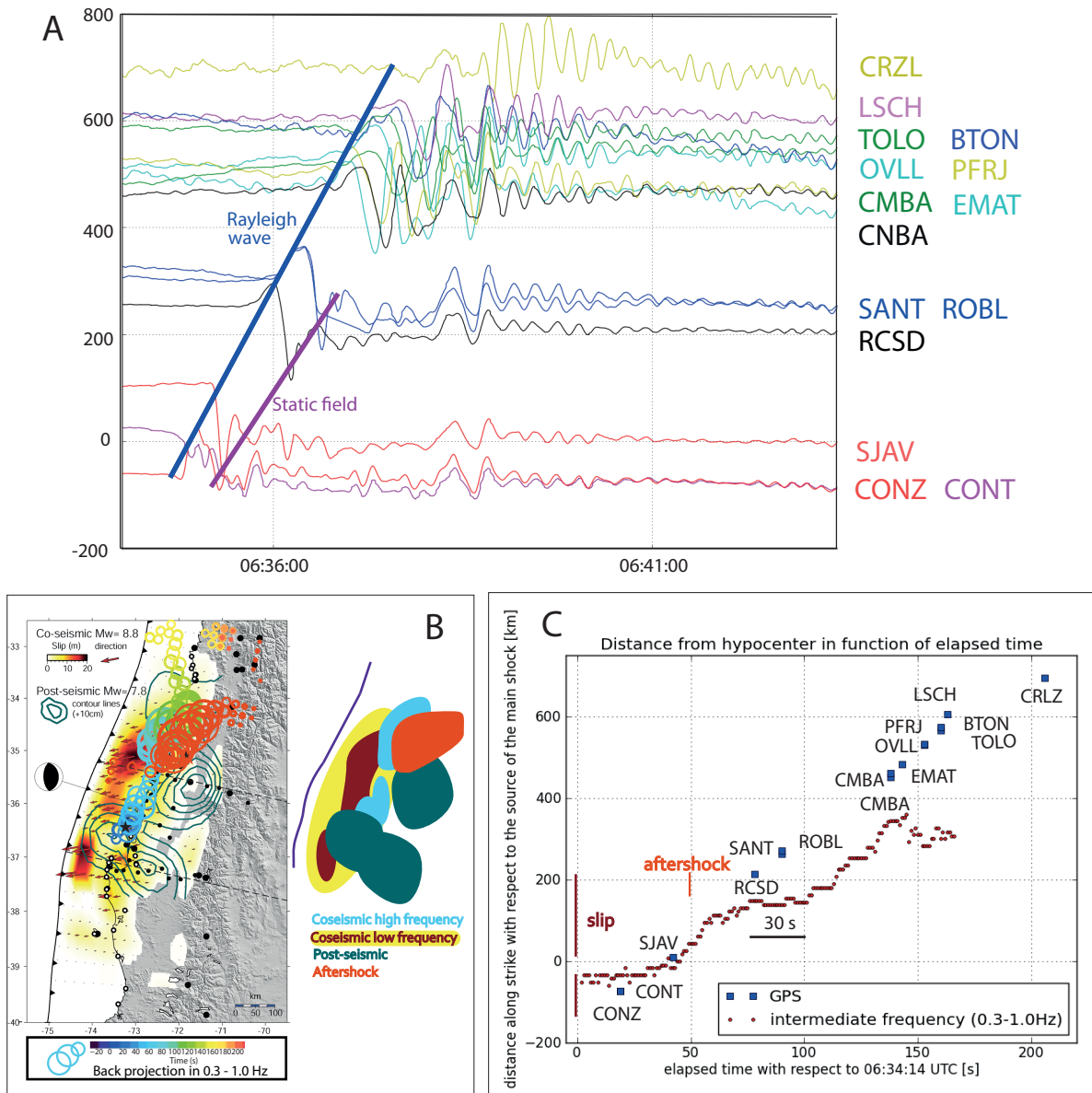
Figure 9 – Vertical cGPS components showing Rayleigh wave arrival and installation of static field. Horizontal axis shows the UTC time, vertical axis indicates the distance along strike from the epicenter in km (panel top A). Superposition of GPS coseismic slip (redish-yellowish patches), post-seismic activity (blue contours), short-period radiation of the main shock calculated with back projection (blue-green circles) and the 25 March 2012 aftershock (red circles). See schema next to the map (panel left bottom B). Time evolution of short-period radiation (red dots) and cGPS observations (blue squares). Coseismic slip and aftershock location is indicated with vertical bars. Black horizontal bar indicate the time delay between the short-period radiation and cGPS arrivals from about 70s (panel right botoom C)

jection results. Furthermore, broadband data of seismograms in Peldeue should be involved which can give new insights to the near field observations.

3 The 2012 Mw 8.6 Sumatra earthquake: evidence of westward sequential seismic ruptures associated to the reactivation of a N-S ocean fabric

Claudio Satriano, Eszter Kiraly, Pascal Bernard and Jean-Pierre Vilotte

3.1 Abstract

The 11 April 2012 Mw 8.6 earthquake offshore Sumatra is the largest of the rare great intraplate earthquakes of the instrumental era. This major strike-slip event occurred in the diffuse zone of deformation that accommodates differential rotation between Indian and Australian plates. We perform a back projection analysis – calibrated with well-located aftershocks – of short-period teleseismic P-waves recorded by the European array to image the rupture process during the mainshock. In complement, a Love wave analysis is conducted for tracking azimuthal change in the apparent global source duration due to the source spatio-temporal extent. The combined analysis reveals a complex rupture pattern, characterized by three main episodes of energy release, the latest being located 370 km west of the epicenter, on the Ninety East Ridge, with a delay of 120 s. We interpret the 11 April 2012 Mw 8.6 offshore Sumatra earthquake as a complex westward-propagating sequence of dynamically triggered strike-slip fault ruptures, associated to the reactivation of the inherited NNE–striking sea floor fabric. The dynamic triggering mechanism could result from the interaction between transient surface wave stress perturbations and fluids.

3.2 Introduction

On 11 April 2012, a great Mw 8.6 earthquake occurred in the Wharton Basin, 100 km southwest of the Sumatra Trench, and was followed by a major Mw 8.2 aftershock two hours later (Figure 10). These events belong to the diffuse deformation zone of the Indian Ocean that extends between the Chagos-Laccadive Ridge and the Sumatra Trench, accommodating the relative rotation between the Indian and the Australian plates [Wiens et al., 1985]. In this region, the Ninety East Ridge (90ER) acts as mechanical boundary between compressive deformation to the west and strike-slip deformation to the east.

The Wharton Basin (WB) – east of the 90ER – is a wide oceanic left-lateral shear band striking N-S, and characterized by an inherited complex fracture zone originating from the extinct Wharton spreading ridge [Deplus et al., 1998]. The diffuse intra-plate seismicity in this region results predominantly from the reactivation of N-S–trending left-lateral strike-slip faults of the fracture zone fabric [Delescluse and Chamot-Rooke, 2007], which can produce large earthquakes, like the 2000 June 18 (Mw 7.9) WB earthquake [Robinson et al., 2001, Abercrombie et al., 2003].

The two 2012 April 11 events are characterized by a predominant strike-slip, left lateral mechanism. The centroid depth range of 18-27 km of the mainshock, determined by the SCARDEC method [Vallée et al., 2010], suggests major rupture involving the brittle portion of the mantle. Focal mechanisms and locations are in agreement with the active deformation and the inherited sea floor fabric.

A number of preliminary kinematic inversions of the April 2012, Mw 8.6 mainshock (see references in the Auxiliary Material) identify the NNE-SSW nodal plane as the preferred rupture plane, based on aftershock location, optimized fit of waveforms, and orientation of the
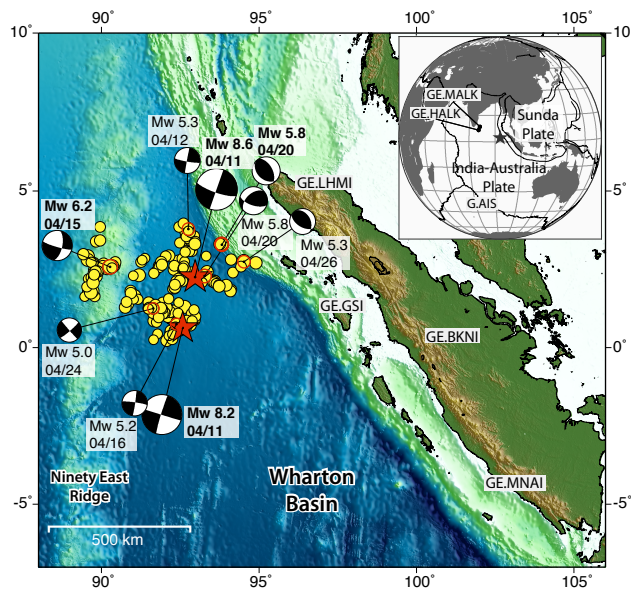
Figure 10 – The 2012 Sumatra sequence, showing the first 28 days of aftershocks. The two largest events are indicated by red stars; others are represented by yellow circles. Relocated epicenters and revised moment tensor solutions from GEOFON (http://geofon.gfz-potsdam.de/eqinfo/special/gfz2012hdex). The events discussed in the text are in bold. Bathymetry from Ryan et al. [2009]. Stations used for the surface wave analysis (Figure 13) are shown on the main map (GE.LHMI, GE.GSI, GE.BKNI, GE.MNAI), and on the inset (GE.MALK, GE.HALK, G.AIS).

fracture zone fabric. The occurrence of aftershocks west of the mainshock epicenter, up to the 90ER (Figure 10), raises however the possibility of a NW-SE rupture plane, or of a more complex rupture. To image the rupture process of the April 11 Sumatra mainshock, we combine: a back projection analysis of short-period (0.1-1.0 Hz) P-waves recorded by the European array, after calibration with well-located aftershocks; a study of apparent source duration, at different distances and azimuths, from long-period (20-50 s) Love waves.

3.3 Back projection analysis

The back projection (BP) method is a beam forming approach that tracks back the observed coherent short period seismic radiation to the most likely source on the fault plane, [e.g., Ishii et al. 2005b]. Those short-period radiation sources, when imaging extended earthquake ruptures (e.g., M>8 events at teleseismic distance), are not necessarily co-located with large coseismic slip asperities [e.g., Satriano et al. 2011, Lay et al. 2012b], reflecting dynamical complexities due to geometrical or mechanical heterogeneities.

We use a BP method [Satriano et al., 2011] similar to that of Xu et al. [2009]. The data set is composed of 204 vertical velocity components of the Virtual European Broadband Seismograph Network (VEBSN, Figure 2a) [van Eck et al., 2004]. The BP analysis is performed in two frequency bands, 0.1-0.5 Hz and 0.5-1.0 Hz. Travel times are computed using a 1D global velocity model (AK135) [Kennett et al., 1995]. A 4-th root stacking technique [Xu et al., 2009] is used to enhance phase coherency over amplitude coherency, improving resolution at the expense of a possible distortion of relative amplitudes of the energy peaks. The epicentral area is discretized using a square grid of 1600 km in size, centered at the mainshock epicenter, with a grid spacing of 20 km (Figures 11b and 11c). At teleseismic distance, the BP method has little or no resolution in depth [e.g., Koper et al. 2012], and the grid is a priori set at depth at 10 km. The BP images are post-processed using a so-called "cube-smoothing" operator, similar
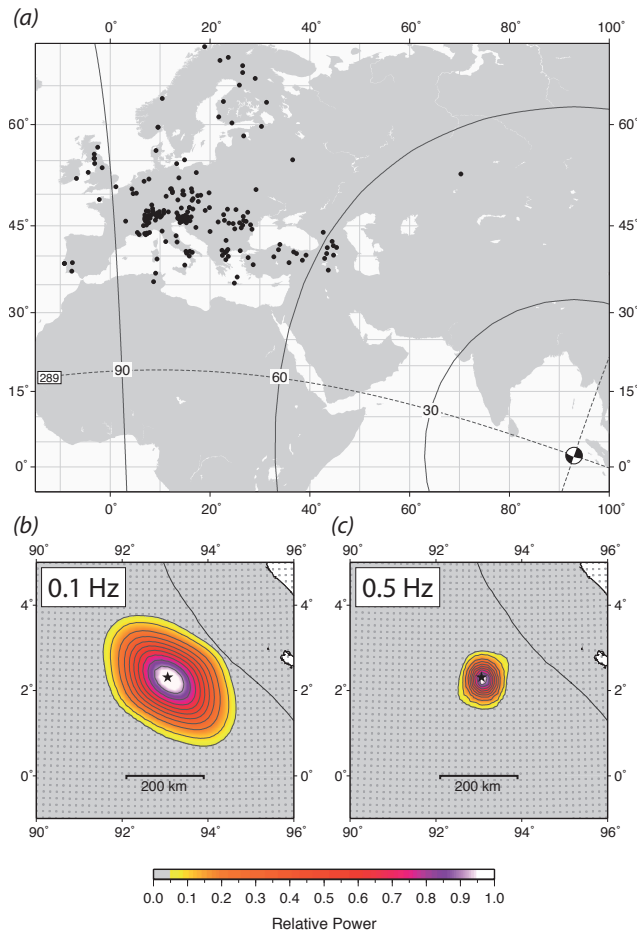
Figure 11 – (a): Location of the stations (black dots) used for the back projection analysis; (b) and (c): Array response functions at 0.1 Hz and 0.5 Hz. Back projection grid notes are indicated by gray dots. Grid spacing is 20 km; grid size is 1600 km x 1600 km (larger than the plot size).

to the one proposed by Walker and Shearer [2009b], to mitigate sweeping artifacts related to non-destructive interference of incoherent energy.

The horizontal resolution of the BP images can be assessed from the evaluation of the array response function (ARF) [Rost and Thomas, 2002]. The ARF is constructed from BP of monochromatic signals delayed across the network according to the relative travel time from the mainshock epicenter. For each band, we use the lower frequency – namely, 0.1 and 0.5 Hz – to estimate the lowest resolution limit. Figures 11b and 11c show the two resulting ARFs, as normalized maximum power plots. At 0.1 Hz, the ARF is distorted in the direction of the VEBSN (SE-NW), while at 1.0 Hz the ARF does not show significant distortions.

The departure from 1D velocity model for short period waves – mainly related to lithospheric heterogeneities – cause defocusing of BP images that needs to be corrected. Residual station corrections are calculated by applying multi-channel cross-correlation [Vandecar and Crosson, 1990b] to the first-arrival P waveforms, preliminary aligned according to theoretical travel-times from GEOFON hypocenter (93.14° E, 2.27° N, 10 km depth, origin time: 08:38:35.5 UTC). These station corrections are then used through the whole BP process. The robustness of this calibration step has been verified for two well located aftershocks, as discussed in the auxiliary material.

Results of the back projection for the mainshock – in the 0.1-0.5 Hz and 0.5-1.0 Hz fre-

quency bands – are synthesized in Figure 12. Left panels (Figures 12a and 12c) show the spatial distribution of maximum BP power reached at each grid node during the rupture, as interpolated surface and contour lines. The largest extension of radiative sources is observed for the 0.1-0.5 Hz band, with several radiating episodes between the epicenter area and the 90ER. The maxima of back projected energy are well separated in space, according to the resolution analysis (see Figure 11), and correspond quite well to the aftershock locations (black dots). At higher frequencies (0.5-1.0 Hz), the source appears more compact and mainly concentrated at the epicenter location, with a secondary event to the SW.

Right panels (Figures 12b and 12d) show the spatio-temporal distribution of BP peaks, with amplitude proportional to the relative BP power, and color indicating relative time from the hypocenter. The peaks are extracted using a local maximum filter; therefore multiple local maxima are possible, corresponding to points radiating simultaneously.

The time history in the 0.1-0.5 Hz band shows three main energy events peaking at about 30, 100 and 150 s, and a later, smaller peak at about 190 s. The radiative source remains close to the epicenter location during the first 60-70 s (subevent A on Figure 12b) and then moves northward (subevent B1). At that time, a BP energy radiative source appears to the WSW (subevent B2), about 225 km away from the epicenter. Finally, a third radiative source (subevent C) appears at 120 s, 370 km west of the main source A; this source is followed by a late burst of energy more to the North (subevent D, starting at 170 s). The apparent SE-NW propagation of the energy peaks for each of the subevents is an artifact due to the distortion of the BP images in the direction of the VEBSN, as evidenced from the ARF at 0.1 Hz (Figure 11).

For the 0.5-1.0 Hz band, the BP is mainly sensitive to the epicenter rupture initiation and to the WSW radiation at $\sim$100 s (subevents A and B). The timing is compatible with that of the 0.1-0.5 Hz band. The resolution in this band is higher and the BP images show no significant distortion.

3.4 Surface wave analysis

To find evidence of any long period radiation from the third BP source (subevent C), we analyzed its radiated long period (20-50 s) Love waves at different stations, shown in Figure 10. Subevent C being shifted by 370 km to the West from A, an azimuthal variation of the relative timing of the surface waves arrivals is expected, with shorter delay towards West (directive) and longer delay towards East (antidirective). In particular, for antidirective stations, the expected time difference is of the order of $2 \cdot d/V_g$, where d is the distance between the two BP subevents (A and C) and V_g is the group velocity ($V_g = 4.4$ km/s).

In Figure 13, transverse component of the Love wave associated to the mainshock is plotted, for different azimuthal directions, together with that of an Mw 5.8 aftershock, used as reference Green's function. Stations located in the eastern quadrant from the source (LHMI, GSI, BKNI) clearly show a distinct, secondary event, delayed by about 200-250 s with respect to the first one. In contrast, stations in the western quadrant (HALK and MALK) show a compact surface wave packet, larger than that of the corresponding Green's function – with difference in duration of about 70 s – close to the duration of the first BP source (subevent A). Finally, the station to the South (AIS) shows a secondary radiation with a delay of about 100 s, which is close to the time delay between the BP sources A and C.

These observations are all compatible with a strong, secondary source of surface waves, coinciding with the third source of the BP (subevent C): the calculated theoretical delays between the Love wave packets from subevents A and C are in agreement with the delays measured from the envelopes in Figure 13. This analysis demonstrates that the third BP source
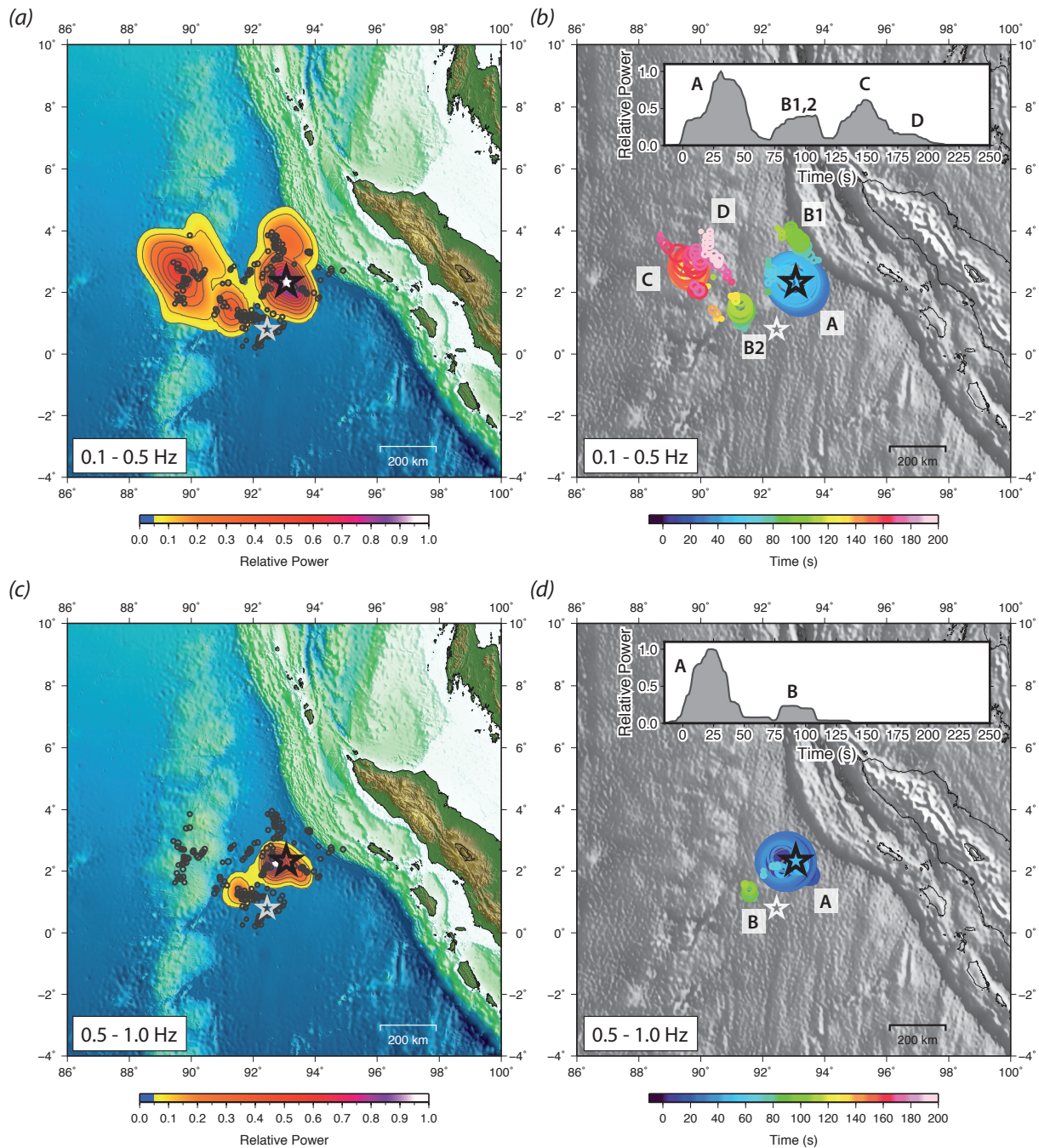
Figure 12 – Back projection results for the Mw 8.6 mainshock. (a) and (c): normalized maximum radiated power in the 0.1-0.5 Hz and 0.5-1.0 Hz frequency bands. Black and white stars are mainshock and largest aftershocks epicenters, respectively; black dots are first 28 days aftershocks. Bathymetry as in Figure 10. (b) and (d): back projection energy peaks colored by elapsed time and scaled by relative normalized power. Shaded background: satellite free-air gravity map [Sandwell and Smith, 2009]. Inlets: maximum back projection relative power on the spatial grid as a function of time.

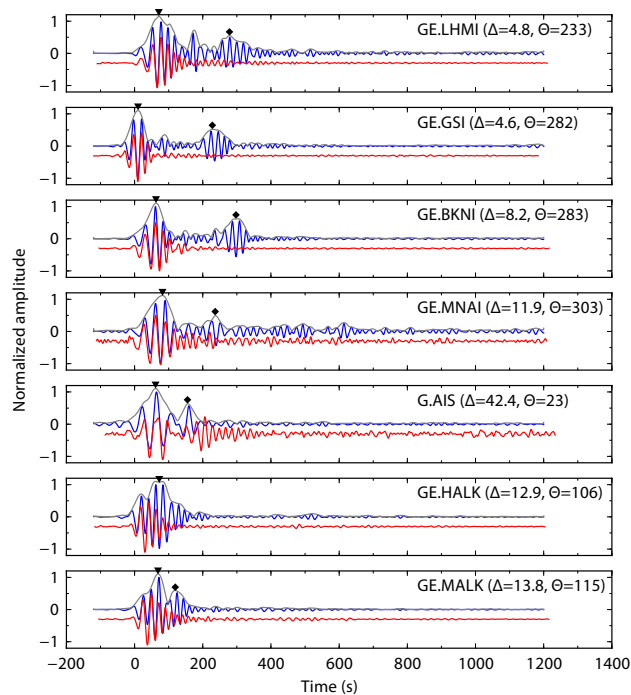Figure 13 – Love waves of the mainshock (blue) and of April 20, Mw 5.8 aftershock (red), from the rotated transverse components filtered between 20 and 50 s. For the mainshock, the trace envelope is shown in gray. Station distance (Δ, degrees) and back-azimuth (Θ, degrees) are indicated after the station name. See Figure 1 for location of events and stations. Triangles and diamonds: observed arrival time of wave packets from subevent A and C, respectively.

(subevent C) radiates energetic surface waves in the 10-50 s period range and is not an artifact of the back projection. The amplitude of Love waves is about 1 to 1.5 larger than those of the Mw 8.2 aftershock, as evidenced on the records of Eastern stations (PSI, KUM, IPM, BTDF), suggesting a similar moment magnitude for source C.

3.5 Interpretation

The back projection analysis reveals an apparent E-W jerky propagation of the radiative sources during the main shock – with three strong subevents – a complex sequence that cannot be explained by simple rupture propagation along a single N-S strike-slip fault.

One hypothesis is to link subevent C to the earlier sources (A or B) through westward rupture propagation along a single fault, conjugate to the sea floor fracture zone fabric. A rupture velocity can be estimated as either ∼3 km/s, from A to C, or ∼3.5 km/s from B to C. This hypothesis is puzzling, since most of the recent large strike-slip intra-plate earthquakes in this region suggest the reactivation of the NNE-trending fracture zone fabric. Even though compound rupture has already been invoked for the 2000 June 18 (Mw 7.9) WB earthquake – ∼2000 km SSW of the 2012 sequence [Robinson et al., 2001, Abercrombie et al., 2003], the main energy release was associated to the reactivation of a fossil N-S–trending strike-slip fault. Example of a large intra-plate earthquake with compound rupture is the great 25 March 1998, Antarctic plate earthquake [Henry et al., 2000, Antolik et al., 2000, Hjörleifsdóttir et al., 2009] involving two conjugate faults.

In the case of the 2012 offshore Sumatra mainshock, a compound rupture mechanism would involve westward rupture propagation over distances of ∼300 km, with weak radiation

in the period range of tens of seconds (and wavelengths of several tens of kilometers), since no energetic surface waves are detected on the eastern stations before the radiation of source C. Such a smooth rupture propagation with a rather uniform slip velocity distribution at this time and space scales, seems unlikely owing to the many NNE-trending fossil strike-slip faults that would crosscut the rupture path at similar scale (see Figure 12) and generate strength heterogeneities.

Another hypothesis is to associate the strong radiation source C to the dynamic triggering of a N-S–trending strike-slip fault by the most energetic surface waves generated from source A. In this case, a 84 s delay is expected – assuming Love wave group velocity of 4.4 km/s and distance of 370 km between A and C – matching very well the observed 95 s delay between the maximum of surface wave radiation from subevent A (30 s) and the start of subevent C (125 s). Furthermore, BP results suggest late northwards rupture propagation along the 90ER, from C to D.

We hence propose that this complex earthquake rupture results from a westward propagating sequence of rapidly triggered ruptures possibly reactivating inherited NNE-trending strike faults (sources B and C) at the passage of the surface waves generated from the early phase of the rupture (source A). This is also supported by the prevalent SSW-NNE alignment of manually revised aftershock locations, in particular for the latest part of the rupture on the 90E Ridge (Figure 10). This model does not exclude the possibility of some diffuse and smooth E-W rupture components along conjugate strike-slip faults at local scales, that might not be resolved by the back projection analysis.

3.6   Discussions and conclusions

Since the classical Joshua Tree-Landers-Hector Mine sequence [Parsons and Dreger, 2000], dynamic stress transfer has been proposed as potential mechanism to enable delayed jumps of the rupture across distant fault segments, and to trigger remote seismicity at large distances, [e.g., Hill et al. 1993, Hough and Kanamori 2002]. However, evidence of rapid dynamic stress triggering during a single large earthquake event has rarely been reported.

Sequence of dynamically triggered fault ruptures during a single event has been recently observed for the 29 May 2008 (Mw 6.2) earthquake [Hreinsdóttir et al., 2009], in the South Icelandic Seismic Zone, and for the great 25 March 1998 (Mw 8.1) Antarctic earthquake [Henry et al., 2000, Antolik et al., 2000, Hjörleifsdóttir et al., 2009] possibly involving two triggered fault segments at 100 km distance.

At the period of tens of seconds, the triggering potential of Love and Rayleigh waves remains large within the whole depth range of the 2012 Sumatra earthquake. Their combined effects can trigger instantaneous rupture initiation under mixed mode condition [Hill, 2008]. Transient shear stress perturbation, induced by the Love waves, is maximal for strike-parallel and strike-normal incidence on vertical NNE-striking strike-slip faults. Rayleigh wave potential is associated to shear and to interaction between transient dilatational stress perturbation and fluids. For periods of ∼20 s, coherent pore pressure oscillation cycles – over length scales of ∼80 km – can lead to transient fault weakening, [e.g., Boettcher and Marone 2004, Hill et al. 1993]. This can be enhanced by the complex fluid pore pressure distributions expected in inherited fracture zone.

Heterogeneous initial stress distribution, suggested by the diffuse seismicity in this region, can control the triggered rupture locations, and the nearly instantaneous rupture initiation. Interestingly enough, no M>5.5 event is reported in the mainshock area between 1965 and the 2004 Sumatra megathrust earthquake (www.isc.ac.uk), while after 2004, three large strike

slip events (Mw 5.6, 2006/04/19; Mw 6.1, 2007/10/04; Mw 7.2, 2012/01/10) occurred within 50 km of the 2012 epicenter, suggesting possible stress re-arrangements induced by the 2004 earthquake.

The 11 April 2012, Mw 8.6 earthquake provides evidence – as revealed by back projection and Love wave analysis – of a complex rupture sequence reactivating inherited NNE-trending left-lateral strike-slip faults of the oceanic fabric. The rupture is characterized by three main episodes: (1) a major rupture, striking dominantly NNE, and lasting 70 s; (2) a weaker and complex westward propagating sequence of ruptures; (3) a late, powerful source after 120 s, lasting ∼80 s, and coinciding with the 90E Ridge, 370 km to the West. The latter source appears to be dynamically triggered at the passage of the large surface waves from the early rupture, and relatively depleted in high frequencies, suggesting possible slow and coherent slip.

Great (M>8) intra-plate strike-slip earthquakes are extremely rare. The 2012 Mw 8.6 Sumatra earthquake is the largest ever recorded, the others being the 1998 Mw 8.1 Antarctic plate earthquake and the 2004 Mw 8.1 Tasman Sea earthquake [Robinson, 2011]. A better understanding of dynamic triggering and fault interaction during such events is a necessary step for assessing the seismic potential associated to possible reactivation of similar inherited fracture systems in other oceanic diffuse plate boundary zones.

This study illustrates once again the importance of teleseismic back projection methods to constrain complex large earthquake rupture, avoiding some of the biases associated with a-priori parameterization. It revealed the late energetic source C, which motivated subsequent surface wave analysis, and provides the main source parameters for future, more complete source analysis, combining body and long period surface waves.

4   Conclusion

Our study of the 2010 Maule and 2012 Sumatra earthquakes showed that broadband analysis can reveal new information about complex source properties and post-seismic activity which have not seen before applying slip inversion techniques as it was reported for the 2011 Tohoku event. Combined investigation of high- and low-frequency energy radiations can improve the understanding on rupture mechanism, propagation, seismic nucleation properties. Application and combination of high-frequency back projection technique, GPS measurements and surface wave analysis give considerable results.

To understand the northern ending of the 27 February 2010 Maule (Mw 8.8) earthquake cGPS first arrival observation, coseismic slip, afterslip (calculated from GPS measurements) and high-frequency coherent energy radiation were combined in this study. Regions radiating at different frequencies were positioned: low-frequency coseismic slip is located close to the trench [Vigny et al., 2011]; dominant coherent coseismic high-frequency radiated downdip around the hypocenter and about 250km further to the north; and significant post-seismic activity occurred between the two high-frequency patches deeper on the subduction interface. These regions encircle an area which was probably strongly coupled. Decoupling of short-period coherent coseismic radiation also confirms that the asperity was highly coupled and breaking of little asperities recharged the area. The 25 March 2012 aftershock (Mw 7.1) occurred and released at least a part of the accumulated energy.

The largest ever recorded intra-plate strike-slip earthquake occurred on 11 April 2012 (Mw 8.6) offshore from Sumatra. A complex rupture sequence was detected by investigating with short-period back projection and long-period surface wave analysis. The earthquake reactivated inherited NNE-SSW trending left-lateral strike slip oceanic faults in three separated episodes. Understanding of dynamic triggering and fault interaction can provide new element

of seismic potential of other diffuse plate boundary regions.

In conclusion, broadband analysis of great earthquakes, including back-projection techniques, can give new elements of the seismic activity and potential of different areas. Thus, past and future large earthquakes need to be (re)analyzed with broadband approach.

5 Appendix

$$S_i(t) = \sum_{k=1}^{n} a_k u_k(t - t_{ik}^P + dt_k) \tag{1}$$

where n indicates the number of seismograms, $s_i(t)$ is the stacked trace at the ith grid point in function of time, u_k is the real seismogram, a_k is a weight of the kth station, t_{ik}^P is the predicted time between the grid point i and station k, dt_k is the time shift obtained from cross correlation.

$$B(t) = \frac{1}{M} \sum_{k=1}^{n} |b_j(t)|^{1/N} sign(b_j(t)) \tag{2}$$

$$BP(t) = |B(t)|)^N sign(B(t)) \tag{3}$$

where BP is the final beam power, B is an intermediate stack, N refers to the Nth root stacking, $b_j(t)$ is the amplitude of the jth trance, M is the number of seismograms.

6 Acknowledgement

References

Rachel E Abercrombie, Michael Antolik, and Göran Ekström. The June 2000 Mw7.9 earthquakes south of Sumatra: Deformation in the India–Australia Plate. *J. Geophys. Res.*, 108(B1), 2003.

Michael Antolik, Asya Kaverina, and Douglas S Dreger. Compound rupture of the great 1998 Antarctic plate earthquake. *J. Geophys. Res.*, 105(B10):23825–23838, 2000.

S. Beck, S. Barrientos, E. Kausel, and M. Reyes. Source characteristics of historic earthquakes along the central chile subduction zone. *Journal of South American Earth Sciences, 11, 115*, 1998.

M S Boettcher and C. Marone. Effects of normal stress variation on the strength and stability of creeping faults. *J. Geophys. Res.*, 109(B3), 2004.

D. Campos J.and Hatzfeld, R. Madariaga, G. Lopez, E. Kausel, A. Zollo, G. Iannacone, R. Fromm, S. Barrientos, , and H. Lyon-Caen. A seismological study of the 1835 seismic gap in south-central chile. *Phys. Earth Planet. Inter., 132(1–3):177–195*, 2002.

D. Comte, Eisenberg A., Lorca E., Pardo M., Ponce L., Saragoni R., Singh SK, and G. Suarez. The 1985 central chile earthquake: A repeat of previous great earthquakes in the region ? *Science, 233(4762):449, 1986*, 1986.

S. Das and C. Henry. Spatial relation between main earthquake slip and its aftershock distribution. *Rev. Geophys., 41(3), 1013*, doi:10.1029/2002RG000119, 2003.

Matthias Delescluse and Nicolas Chamot-Rooke. Instantaneous deformation and kinematics of the India-Australia Plate. *Geophys. J. Int.*, 168(2):818–842, February 2007.

B. Delouis, J.-M. Nocquet, and M. Vallee. Slip distribution of the february 27, 2010, mw = 8.8 maule earthquake, central chile, from static and highrate gps, insar, and broadband teleseismic data. *Geophys.Res. Lett., 37, L17305*, doi:10.1029/2010GL043899, 2010.

Christine Deplus, M. Diament, H Hébert, G. Bertrand, S. Dominguez, J. Dubois, J. Malod, P. Patriat, B. Pontoise, and J.J. Sibilla. Direct evidence of active deformation in the eastern Indian oceanic plate. *Geol*, 26(2):131–134, 1998.

V. Dionicio, C. Satriano, E. Kiraly, J.-P. Vilotte, and P. Bernard. Broadband characterization of large subduction earthquakes through the combination of coherent rupture imaging and kinematic modeling. *Geophysical Research Abstracts, Vol. 14, EGU2012-8546, 2012 EGU General Assembly 2012*, 2012.

C. Henry, Shamita Das, and JH Woodhouse. The great March 25, 1998, Antarctic Plate earthquake: moment tensor and rupture history. *J. Geophys. Res.*, 105(B7):16097–16118, 2000.

D P Hill, P A Reasenberg, A Michael, W J Arabaz, G Beroza, D Brumbaugh, J N Brune, R Castro, S Davis, D dePolo, W L Ellsworth, J Gomberg, S Harmsen, L House, S M Jackson, M J S Johnston, L Jones, R Keller, S Malone, L Munguia, S Nava, J C Pechmann, A Sanford, R W Simpson, R B Smith, M Stark, M Stickney, A Vidal, S Walter, V Wong, and J Zollweg. Seismicity Remotely Triggered by the Magnitude 7.3 Landers, California, Earthquake. *Science*, 260(5114):1617–1623, June 1993.

David P Hill. Dynamic Stresses, Coulomb Failure, and Remote Triggering. *Bull. Seismol. Soc. Am.*, 98(1):66–92, February 2008.

Vala Hjörleifsdóttir, Hiroo Kanamori, and Jeroen Tromp. Modeling 3-D wave propagation and finite slip for the 1998 Balleny Islands earthquake. *J. Geophys. Res.*, 114(B3), March 2009.

S.E. Hough and Hiroo Kanamori. Source properties of earthquakes near the Salton Sea triggered by the 16 October 1999 M 7.1 Hector Mine, California, earthquake. *Bull. Seismol. Soc. Am.*, 92(4):1281–1289, 2002.

Sigrún Hreinsdóttir, T Árnadóttir, J Decriem, H Geirsson, A Tryggvason, R A Bennett, and P LaFemina. A complex earthquake sequence captured by the continuous GPS network in SW Iceland. *Geophys. Res. Lett*, 36(12), June 2009.

M. Ishii, P. M. Shearer, H. Houston, and J. E. Vidale. Extent, duration and speed of the 2004 sumatra-andaman earthquake imaged by the hi-net array. *Nature Letters Vol 435, 16 June 2005*, doi:10.1038/nature03675, 2005a.

Miaki Ishii, Peter M Shearer, Heidi Houston, and John E Vidale. Extent, duration and speed of the 2004 Sumatra-Andaman earthquake imaged by the Hi-Net array. *Nature*, 435:933–936, June 2005b.

B. Kennett, E. R. Engdahl, and R. Buland. Constraints on seismic velocities in the earth from traveltimes. *Geophys. J. Int., 122(1), 108–124*, doi:10.1111/j.1365- 246X.1995.tb03540.x., 1995.

E. Kiser and M. Ishii. Large extensional aftershocks in the continental forearc triggered by the 2010 maule earthquake, chile. *Geophisical Research Letters, Vol. 38, L07301, 6 PP., 2011*, doi:10.1029/2011GL047140, 2011.

K. Koper, A. R. Hutko, T. Lay, and O. Sufri. Imaging short-period seismic radiation from the 27 february 2010 chile (mw 8.8) earthquake by back-projection of p, pp, and pkikp waves. *J. Geophys. Res., 117(B2)*, doi:10.1029/2011JB008576, 2012.

D. Lange, F. Tilmann, S. E. Barrientos, E. Contreras-Reyes, P. Methee, M. Moreno, B. Heit, H. Agurto, P. Bernard, J-P. Vilotte, and S. Beck. Aftershock seismicity of the 27 february 2010 mw 8.8 maule earthquake rupture zone. *Earth and Planetary Science Letters,Volumes 317–318, 1 February 2012, Pages 413–425*, 2012.

T. Lay, C. J. Ammon, H. Kanamori, K. D. Koper, O. Sufri, and A. R. Hutkoe. Teleseismic inversion for rupture process of the 27 february 2010 chile (mw 8.8) earthquake. *Geophys. Res. Lett., 37, L13301*, doi:10.1029/2010GL0433790, 2010.

T. Lay, H. Kanamori, C. J. Ammon, K. D. Koper, A. R. Hutko, L. Ye, H. Yue, and T. M. Rushing. Depth-varying rupture properties of subduction zone megathrust faults. *J. Geophys. Res., 117, B04311*, 2012a.

Thorne Lay, Hiroo Kanamori, Charles J Ammon, Keith D Koper, Alexander R Hutko, Lingling Ye, Han Yue, and Teresa M Rushing. Depth-varying rupture properties of subduction zone megathrust faults. *J. Geophys. Res.*, 117:B04311, 2012b.

C. Lomnitz. Major earthquakes of chile: A historical survey, 1535-1960. *Seismological Research Letters, 75, 368*, 2004.

S. Lorito, F. Romano, S. Atzori, X. Tong, A. Avallone, J. McCloskey, M. Cocco, E. Boschi, and A. Piatanesi. Limited overlap between the seismic gap and coseismic slip of the great 2010 chile earthquake. *Nat. Geosci., 4, 173âĂŞ177*, doi:10.1038/ngeo1073, 2011.

R. Madariaga, M. Métois, C. Vigny, and J. Campos. Central chile finally breaks. *Sciences Vol. 328 no. 5975 pp. 181-182*, doi: 10.1126/science.1189197, 2010.

M. Métois, A. Socquet, and C. Vigny. Interseismic coupling, segmentation and mechanical behavior of the central chile subduction zone. *J. Geophys. Res., 117, B03406*, J. Geophys. Res., 117, B034068, 2012.

M. Moreno, D. Melnick, M. Rosenau, J. Baez, J. Klotz, O. Oncken, A. Tassara, J. Chen, K. Bataille, M. Bevis, A. Socquet, J. Bolte, C. Vigny, B. Brooks, I. Ryder, V. Grund, B. Smalley, D. Carrizo, M. Bartsch, and H. Hase. Toward understanding tectonic control on the mw 8.8 2010 maule chile earthquake. *Earth and Planetary Science Letters 321-322 (2012) 152âĂŞ165*, doi:10.1016/j.epsl.2012.01.0066, 2012.

Tom Parsons and Douglas S Dreger. Static-stress impact of the 1992 Landers earthquake sequence on nucleation and slip at the site of the 1999 M= 7.1 Hector Mine earthquake, southern California. *Geophys. Res. Lett*, 27(13):1949–1952, 2000.

A. Rietbrock, I. Ryder, G. Hayes, C. Haberland, D. Comte, S. Roecker, and H. Lyon-Caen. Aftershock seismicity of the 2010 maule mw=8.8, chile, earthquake: Correlation between co-seismic slip models and aftershock distribution? *Geophys. Res. Lett., 39, L08310*, doi:10.1029/2012GL051308, 2012.

David P Robinson. A rare great earthquake on an oceanic fossil fracture zone. *Geophys.J. Int., 186(3), 1121–1134, doi:10.1111/j.1365-246X.2011.05092.x.*, 2011.

David P Robinson, C. Henry, Shamita Das, and JH Woodhouse. Simultaneous rupture along two conjugate planes of the Wharton Basin earthquake. *Science*, 292(5519):1145–1148, 2001.

Sebastian Rost and Christine Thomas. Array seismology: Methods and applications. *Rev. Geophys.*, 40(3):1008, January 2002.

J. C. Ruegg, A. Rudloff, C. Vigny, R. Madariaga, J. B. De Chabalier, J. Campos, E. Kausel, S. Barrientos, and D. Dimitrovy. Interseismic strain accumulation measured by gps in the seismic gap between constitución and concepción in chile. *Phys. Earth Planet. Inter., 175, 78*, 2009.

William B F Ryan, Suzanne M Carbotte, Justin O Coplan, Suzanne O'Hara, Andrew Melkonian, Robert Arko, Rose Anne Weissel, Vicki Ferrini, Andrew Goodwillie, Frank Nitsche, Juliet Bonczkowski, and Richard Zemsky. Global Multi-Resolution Topography synthesis. *Geochem. Geophys. Geosyst.*, 10(3), 2009.

I. Ryder, R. Rietbrock, K. Kelson, R. Burgmann, M. Floyd, A. Socquet, C. Vigny, and D. Carrizo. Large extensional aftershocks in the continental forearc triggered by the 2010 maule earthquake, chile. *Geophys. J. Int., 188(3), 879*, doi:10.1111/j.1365-246X.2011.05321.x, 2012.

David T Sandwell and Walter H F Smith. Global marine gravity from retracked Geosat and ERS-1 altimetry: Ridge segmentation versus spreading rate. *J. Geophys. Res.*, 114(B1), January 2009.

C. Satriano, V. Dionicio, and Vilotte J.-P. Imaging the earthquake rupture from the back projection of body waves. *Geophysical Research Abstracts, 13, EGU2011–11924, 2011*, 2011.

C. Satriano, E. Kiraly, P. Bernard, and J-P Vilotte. The 2012 mw 8.6 sumatra earthquake: evidence of westward sequential seismic ruptures associated to the reactivation of a n-s ocean fabric. *Geophysical Research Letters*, in review, 2012.

X. Tong, D. Sandwell, K. Luttrell, B. Brooks, M. Bevis, M. Shimada, J. Foster, R. Smalley Jr., H. Parra, J.C.B. Soto, M. Blanco, E. Kendrick, J. Genrich, and D.J Caccamise II. Maule, chile earthquake: Downdip rupture limit revealed by space geodesy. *Geophys. Res. Lett., 37, L24311*, doi:10.1029/2010GL045805, 2010.

Martin Vallée, J Charléty, A M G Ferreira, Bertrand Delouis, and J Vergoz. SCARDEC: a new technique for the rapid determination of seismic moment magnitude, focal mechanism and source time functions for large earthquakes using body-wave deconvolution. *Geophys. J. Int.*, 184(1):338–358, November 2010.

Torild van Eck, Chad Trabant, Bernard Dost, Winfried Hanka, and Domenico Giardini. Setting up a virtual broadband seismograph network across Europe. *Eos Trans. AGU*, 85(13):125, 2004.

J. Vandecar and R. S. Crosson. Determination of teleseismic relative phase arrivaltimes using multi-channel cross-correlation and least squares. *Bull. Seismol. Soc. Am.,80(1), 150*, 1990a.

J C Vandecar and Robert S Crosson. Determination of teleseismic relative phase arrival times using multi-channel cross-correlation and least squares. *Bull. Seismol. Soc. Am.*, 80(1):150, February 1990b.

C. Vigny, A. Rudloff, J. C. Ruegg, R. Madariaga, J. Campos, and M. Alvarez. Upper plate deformation measured by gps in the coquimbo gap, chile. *Phys. Earth Planet. Inter.*, 175(1-2): 86–95, 2009.

C. Vigny, A. Socquet, S. Peyrat, J.-C. Ruegg, M. Métois, R. Madariaga, S. Morvan, M. Lancieri, R. Lacassin, J. Campos, D. Carrizo, M. Bejar-Pizarro, S. Barrientos, R. Armijo, C. Aranda, M.-C. Valderas-Bermejo, I. Ortega, F. Bondoux, S. Baize, H. Lyon-Caen, A. Pavez, J. P. Vilotte, M. Bevis, B. Brooks, R. Smalley, H. Parra, J.-C. Baez, M. Blanco, S. Cimbaro, and E. Kendrick.

The 2010 Mw 8.8 maule megathrust earthquake of Central Chile, monitored by GPS. 332 (6036):1417–1421, 2011. doi: 10.1126/science.1204132.

K. T. Walker and P. M. Shearer. Illuminating the near-sonic rupture velocities of the intracontinental kokoxili mw 7.8 and denali fault mw 7.9 strike-slip earthquakes with global p wave back projection imaging. *J. Geophys. Res., 114, B02304*, doi:10.1029/2008JB005738, 2009a.

Kristoffer T Walker and Peter M Shearer. Illuminating the near-sonic rupture velocities of the intracontinental Kokoxili Mw7.8 and Denali fault Mw7.9 strike-slip earthquakes with global P wave back projection imaging. *J. Geophys. Res.*, 114(B2):B02304, February 2009b.

Douglas A Wiens, Charles DeMets, Richard G Gordon, Seth Stein, D. Argus, J.F. Engeln, P Lundgren, D. Quible, Carol A Stein, and S. Weinstein. A diffuse plate boundary model for Indian Ocean tectonics. *Geophys. Res. Lett*, 12(7):429–432, 1985.

Y. Xu, K. D. Koper, O. Sufri, L. Zhu, and A.R. Hutko. Rupture imaging ofthe mw 7.9 12 may 2008 wenchuan earthquake from back projection of teleseismic p waves. *Geochem. Geophys. Geosyst., 10(4), Q04,006*, doi:10.1029/2008GC002335, 2009.